Supplementary information for:

Near-field misalignment-robust real-domain Fourier ptychographic microscopy with spherical-wave forward model and micro-LED array illumination

Mikołaj Rogalski[1,†]Maksymilian Chlipała[1,†], Marzena Stefaniuk[2], Grzegorz Olszak[3], Adam Kłosin[3], Yefeng Shu[4,5,6], Jiasong Sun[4,5,6], Chao Zuo[4,5,6], Maciej Trusiak[1,*], Piotr Zdańkowski[1,*]

[1]Warsaw University of Technology, Institute of Micromechanics and Photonics, Faculty of Mechatronics, Boboli 8, 02-525, Warsaw, Poland

[2]Laboratory of Neurobiology, Nencki Institute of Experimental Biology of Polish Academy of Sciences, BRAINCITY, Warsaw, Poland

[3]Spatial Epigenetics Laboratory, Nencki Institute of Experimental Biology Polish Academy of Sciences

[4]Smart Computational Imaging Laboratory (SCILab), Nanjing University of Science and Technology, Nanjing, Jiangsu 210094, People's Republic of China

[5]Smart Computational Imaging Research Institute (SCIRI), Nanjing University of Science and Technology, Nanjing, Jiangsu Province 210019, People's Republic of China

[6]Jiangsu Key Laboratory of Spectral Imaging and Intelligent Sense, Nanjing, Jiangsu 210094, People's Republic of China

[†]These authors contributed equally: Mikołaj Rogalski, Maksymilian Chlipała

*Correspondence: maciej.trusiak@pw.edu.pl, piotr.zdankowski@pw.edu.pl

1. Illumination module in μFPM system

Figure S1 presents photographs of the illumination module of the μFPM setup, including the linear and rotational stages used for precise positioning of the μLED array. In its current proof-of-concept implementation, the system appears relatively bulky; however, the majority of its volume is occupied by the heat dissipation components, control electronics, and mechanical positioning modules. It is important to emphasize that the conventional optomechanical stages and large thermal radiator were employed strictly for experimental flexibility and alignment mapping during this development phase. In principle, this bulky hardware, particularly the thermal radiator, which is a significant overdesign for the minimal thermal load of the 2.56 × 1.92 mm μLED chip, is unnecessary for a functional system. Transitioning this proof-of-concept into a true on-chip platform will simply require replacing these lab-bench workarounds with static, integrated optoelectronics and standard, low-profile micro-cooling solutions. With a fixed and pre-

calibrated µLED position, and further miniaturization of the thermal management and control electronics, the illumination module itself could be potentially reduced to a volume of only a few cubic centimeters and positioned directly beneath the sample plane.

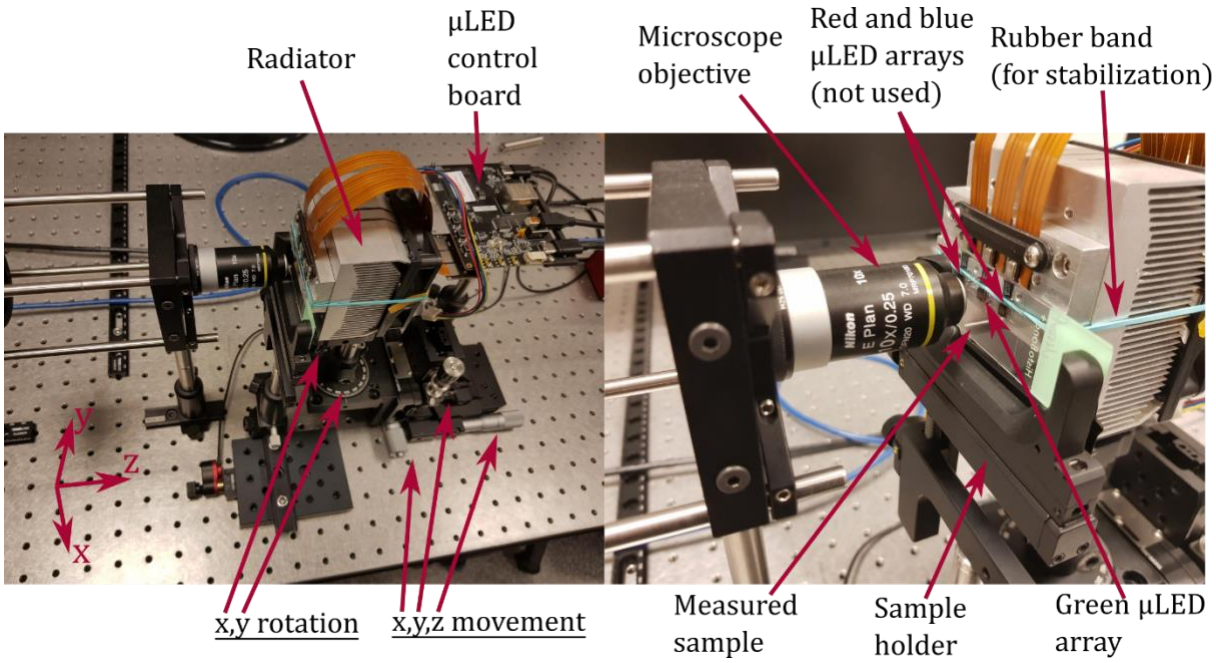

Fig. S1. Photographs of the proof-of-concept µFPM illumination module with labeled components. Underlined elements indicate the linear and rotational stages used for hardware-based µLED calibration, enabling translation along the x, y, and z axes and rotation about the x and y axes. Rotation about the z axis is compensated by adjusting the camera orientation.

2. Influence of d_{LED} parameter on the µFPM performance

The brightness of images acquired in the µFPM system can be controlled, among other factors, by the diameter of the synthetic LED emitters, denoted as d_{LED}. However, increasing d_{LED} also enlarges the effective area of the illumination source, potentially violating the point-source approximation assumed in the rdFPM forward model. Experimentally, variations in d_{LED}manifest primarily as changes in the smoothness of the brightfield–darkfield transition in the raw input images. This effect can be effectively modeled in reconstruction by adjusting the pupil-smoothing parameter $\sigma_{\hat{P}}$ (see Fig. 2 in the main manuscript), which controls the effective sharpness of the illumination support in the frequency domain.

Figure S4 analyzes the influence of d_{LED} on the reconstruction results. For this purpose, two rdFPM+IIC reconstructions were performed using experimental datasets acquired with $d_{LED} = 21$px (Fig. S4(a); the value used for all experimental results in the main manuscript) and with $d_{LED} = 53$px (Fig. S4(b); the maximum achievable diameter in the adopted convention of dividing µLED array into 9x9 synthetic LEDs). Figures S4(a1) and S4(b1) present mosaics of the corresponding input datasets. Figures S4(a2) and S4(b2) show brightfield images acquired under on-axis illumination. The final rdFPM+IIC amplitude reconstructions, obtained using $\sigma_{\hat{P}} = 15$ and $\sigma_{\hat{P}} = 40$, respectively, are shown in Figs. S4(a3) and S4(b3). As can be observed, both datasets yield reconstructions of very similar qualitative accuracy and achieve the same lateral resolution (USAF group 10, element 3, corresponding to a feature size of 0.39 µm). These results indicate

that, within the tested range, the d_{LED} parameter does not impose significant limitations on the rdFPM reconstruction model. Its influence can be effectively compensated by appropriately adjusting the single parameter $\sigma_{\hat{P}}$.

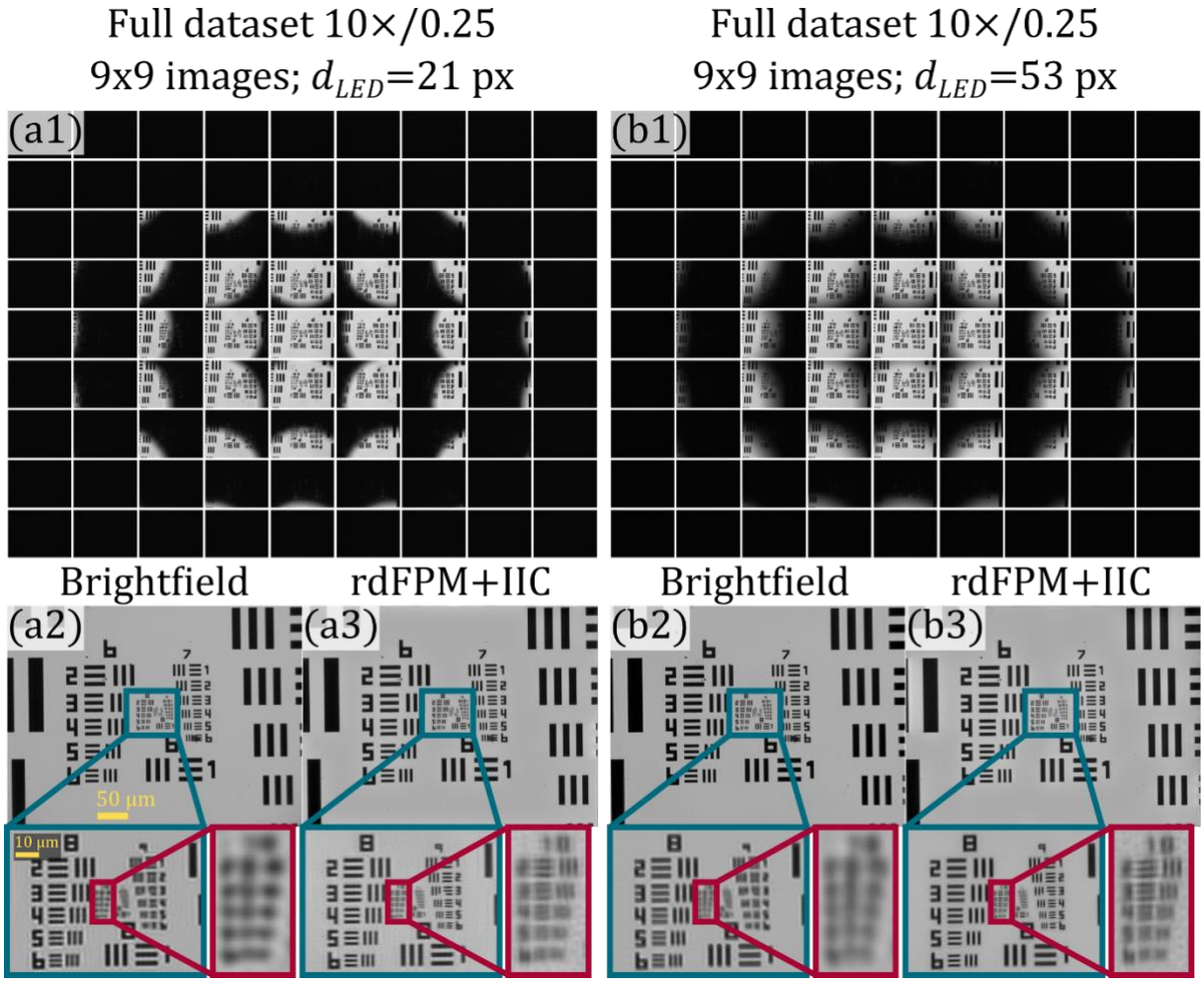

Fig. S2. Amplitude reconstructions of an experimental USAF target acquired with (a) $d_{LED} = 21$ px (value used in all experiments in the main manuscript) and (b) $d_{LED} = 53$ px (maximum value achievable in our system). (a1), (b1) Mosaics of the corresponding input datasets, showing a smoother brightfield–darkfield transition for the larger d_{LED}. (a2), (b2) Brightfield images obtained under on-axis illumination. (a3), (b3) rdFPM+IIC amplitude reconstructions. Both reconstructions exhibit comparable qualitative accuracy and resolution, indicating robustness of the method over a relatively wide range of d_{LED} values.

3. Border errors in rdFPM

The forward model used in rdFPM is described by the Equation (2) from the main manuscript:

$$I_n(x,y) = \left| \boldsymbol{\mathcal{F}^{-1}} \left\{ \boldsymbol{\mathcal{F}} \left\{ \left(E_{obj}(x,y) \cdot \psi_n(x,y) \right) \right\} \cdot \hat{P}(u,v) \right\} \right|^2, \qquad \text{Eq. (2)}$$

where E_{obj} denotes the complex optical field of the object, ψ_n represents the illumination wavefront corresponding to the n-th source, $\hat{P}$ s the system pupil function in the spatial-frequency

domain, I_n is the measured intensity image and $\boldsymbol{\mathcal{F}}$ and $\boldsymbol{\mathcal{F}^{-1}}$ denote the Fourier transform and inverse Fourier transform, respectively.

In the numerical implementation of rdFPM, the discrete Fourier transform (DFT) is employed. The DFT implicitly assumes periodic boundary conditions, meaning that the discrete input signal is treated as one period of a periodically extended function. When plane-wave illumination is used (Eq. (3) in the main manuscript), the illumination factor ψ_n is itself spatially periodic over the computational grid (Fig. S2(a)). Consequently, the periodic extension imposed by the DFT does not introduce significant discontinuities at the image boundaries, and numerical artifacts are negligible (Figs. S2(b), S2(c)). In contrast, under spherical-wave illumination (Eq. (6) in the main manuscript), ψ_n is no longer periodic over the finite computational window (Fig. S2(d)). The implicit periodic continuation introduced by the DFT therefore creates discontinuities at the image borders, leading to edge artifacts in the simulated intensity image I_n (Fig. S2(f)). These artifacts become particularly problematic in rdFPM-based reconstruction algorithm, where multiplication by ψ_n and Fourier-domain propagation are performed repeatedly during iterative reconstruction.

To mitigate this effect, we pad all measured input intensity images I_n by 50 pixels in each spatial direction prior to reconstruction. After reconstruction, the padded margins are removed. Figs. S2(g)–S2(i) illustrate the impact of this procedure for parameters corresponding to our experimental system (10×/0.25 NA objective, 3.45 µm pixel pitch, 1440×1080 camera resolution, 9×9 LED array with 0.2 mm spacing, $l_z = 1.55$ mm, $\lambda = 535$ nm). Fig. S2(g) shows an example input image after padding. Fig. S2(h) presents the reconstructed amplitude when padding is applied, with the original field of view marked by dashed yellow lines. The residual edge artifacts are largely confined to the padded region (see magnified pink inset), and are removed when the padding is cropped. In contrast, reconstruction without padding (Fig. S2(i)) exhibits visible artifacts directly at the borders of the true field of view (see magnified cyan insets).

These results confirm that zero-padding effectively suppresses DFT-induced boundary artifacts in the spherical illumination regime. The only drawback is a modest increase in computational time. For a dataset of size 1440×1080×81 and a reconstruction grid of 2880×2160 pixels (increased to 1540×1180×81 and 3080×2360 pixels after padding), the total reconstruction time increased from 4.38 s to 5.95 s when executed on an NVIDIA GeForce RTX 4070 Laptop GPU.

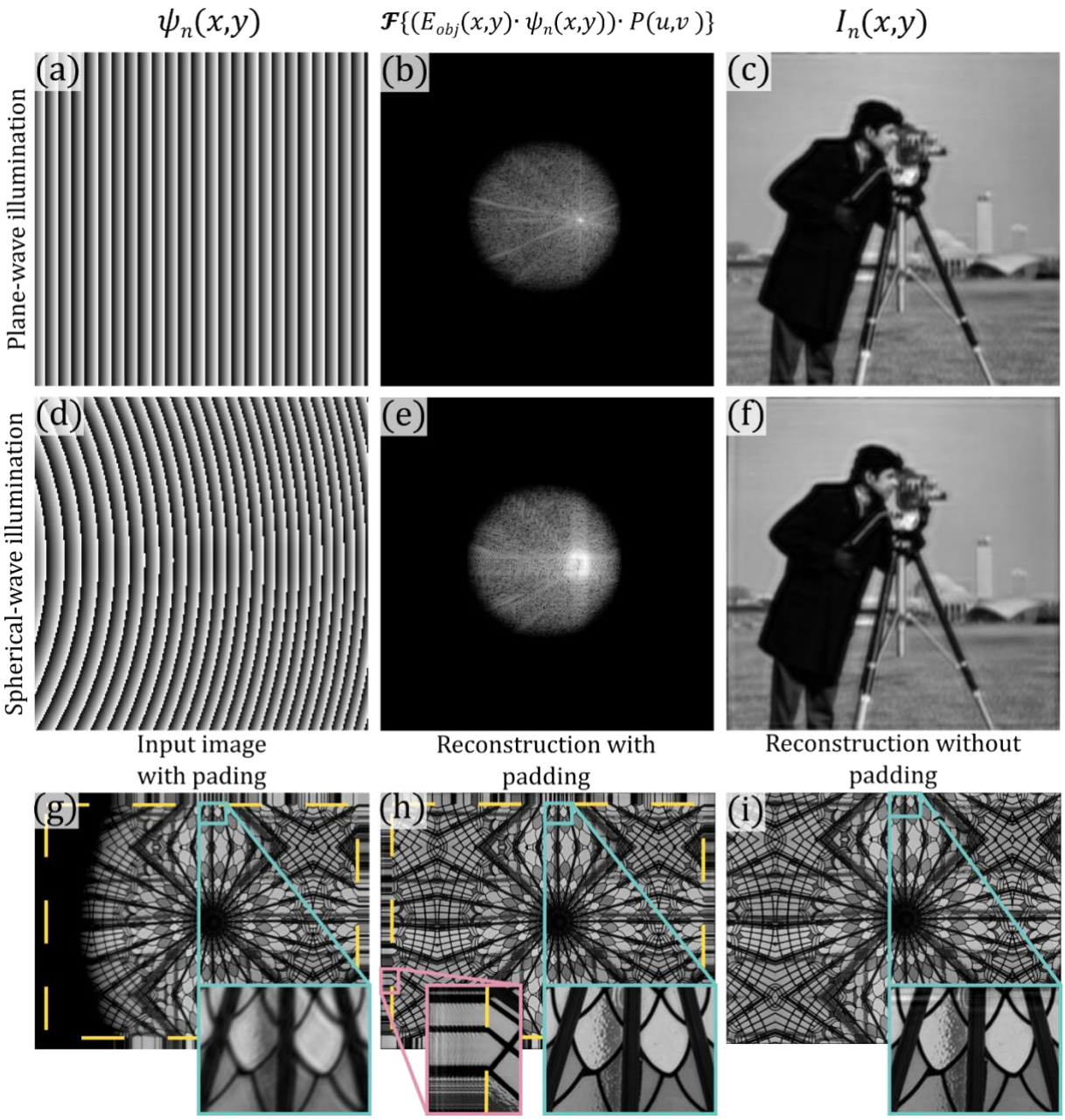

Fig. S3. (a)–(c) Phase of ψ_n illumination wavefront, Fourier transform of the optical field at the camera plane, and simulated intensity image, respectively, for the plane-wave illumination model. (d)–(f) Corresponding quantities for the spherical-wave illumination model. In contrast to the plane-wave case in (c), spherical illumination leads to numerical edge artifacts in the simulated intensity image (f) due to DFT-imposed periodic boundary conditions. (g) Example input image from the FPM dataset (slightly off-axis illumination) after applied padding. (h) rdFPM reconstructed amplitude with padding applied; the original field of view is indicated by dashed yellow lines. (i) rdFPM reconstruction without padding, showing visible boundary artifacts near the image edges.

4. Influence of σ parameter on the IIC reconstruction

The IIC algorithm update step is described by the Equation (12) from the main manuscript:

$$E'_{est\_n}(x,y) = \left(\sqrt{I_n(x,y)} - \langle\sqrt{I_n(x,y)},\sigma\rangle + \langle\left|E_{est\_n}(x,y)\right|,\sigma\rangle\right)\cdot\frac{E_{est\_n}(x,y)}{\left|E_{est\_n}(x,y)\right|}, \qquad \text{Eq. (12)}$$

where E_{est_n} denotes the estimated low-resolution complex field corresponding to the n-th illumination, I_n is the measured low-resolution intensity image, E'_{est_n} is the updated estimate

E_{est_n} and $\langle A(x,y),\sigma\rangle$ represents Gaussian low-pass filtering of matrix A with standard deviation σ.

The updated field E'_{est_n}can be interpreted as a complex field whose phase is preserved from E_{est_n}, while its amplitude is constructed by combining the high-spatial-frequency components of $\sqrt{I_n}$ with the low-spatial-frequency components of $\left|E_{est\_n}\right|$. In other words, the Gaussian filtering acts as a frequency-domain blending mechanism that controls how strongly the measured intensity data influence different spatial frequency bands.

The performance of IIC depends solely on the parameter σ. Larger values of σ correspond to weaker low-pass filtering (i.e., a broader Gaussian kernel), resulting in a stronger contribution of the measured images I_n across a wider spatial-frequency range. In the limit $\sigma \to \infty$, the Gaussian filtering becomes negligible and Eq. (S2) reduces to the standard FPM amplitude replacement step (Eq. (11) in the main manuscript). Conversely, for $\sigma = 0$ (i.e., complete suppression of low-frequency transfer), the measured images I_n are effectively excluded from the update, and no amplitude correction from experimental data is introduced.

Figure S3 investigates the influence of σ on reconstruction quality using the simulated dataset presented in Fig. S9 (for clarity, here only the central part of the reconstructed FOV is shown). Fig. S3(a) presents the reference rdFPM reconstruction obtained for perfectly aligned system parameters. Fig. S3(b) shows rdFPM+IIC reconstructions for misaligned data (with $\Delta l_x = +50$ µm) and various values of σ. Fig. S3(c) presents the corresponding phase root-mean-squared error (RMSE) with respect to the reference reconstruction. For very small values of σ (below 10), the phase reconstructions exhibit reduced accuracy of low-spatial-frequency features. For $\sigma = 0.5$, a noticeable reduction in effective spatial resolution is also observed. In contrast, for very large values of σ (above 100), low-frequency errors caused by system misalignment reappear. These errors are fully visible in the rdFPM-only reconstruction (equivalent to $\sigma \to \infty$; Fig. S3(b7)).

Interestingly, within a broad intermediate range of σ values (approximately 10–100), the reconstruction quality remains highly stable, both qualitatively (Figs. S3(b4), S3(b5)) and quantitatively (Fig. S3(c)). This indicates that the IIC algorithm is not critically sensitive to precise tuning of σ, and any value within this range yields comparable performance. In this work, $\sigma = 20$ was used for all reconstructions.

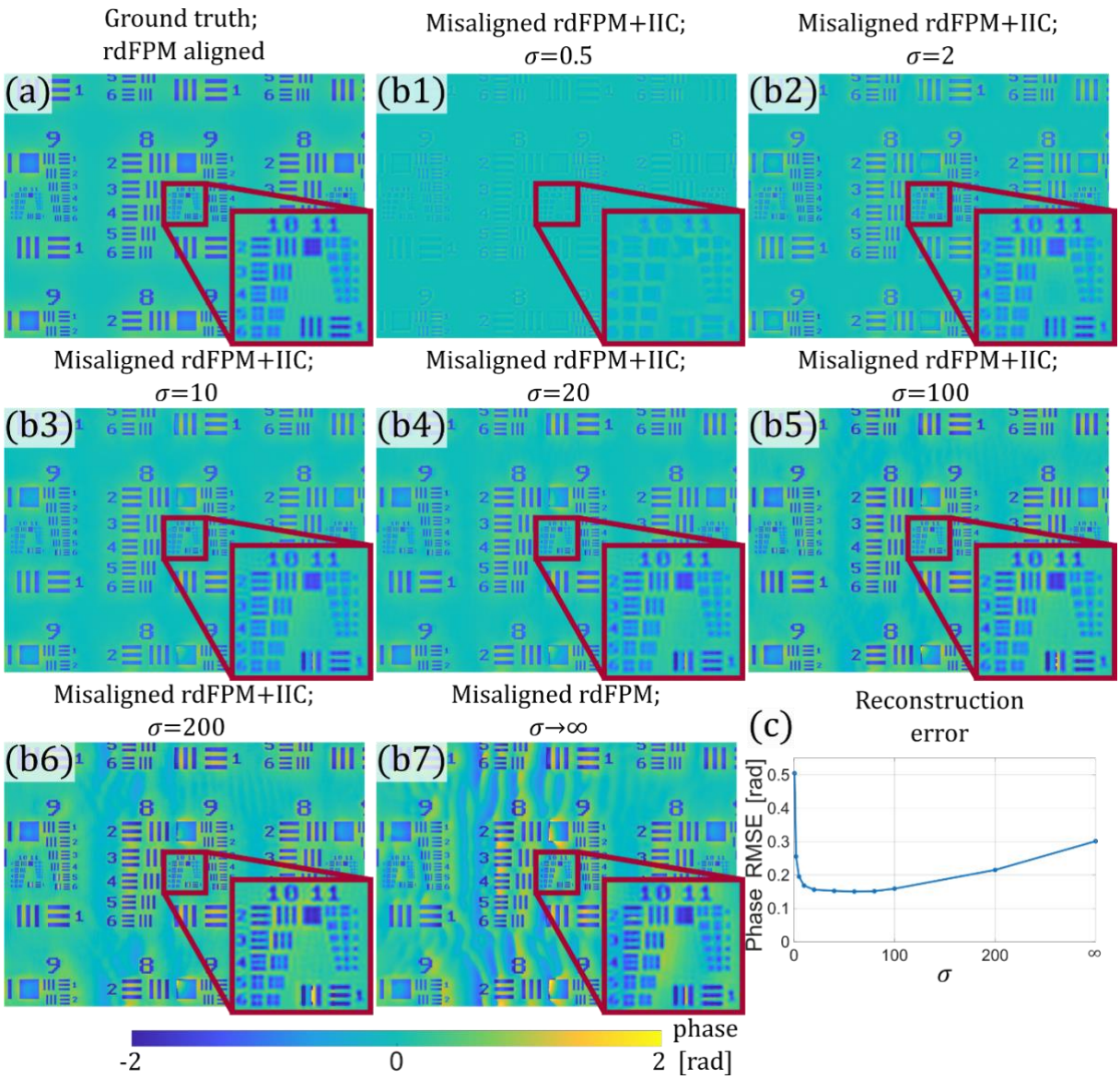

Fig. S4. Reconstructions of simulated USAF targets from Fig. S9. (a) Reference rdFPM reconstruction obtained for perfectly aligned system parameters. (b) rdFPM+IIC reconstructions for misaligned data ($\Delta l_x = +50$ μm) and various values of σ. (c) Phase root-mean-squared error as a function of σ.

5. Influence of PB/PD images presence in dataset

Partially-brightfield/partially-darkfield (PB/PD) images may arise in FPM systems primarily due to (1) vignetting and (2) illumination wavefront sphericity. Their presence in the dataset can lead to significant reconstruction errors, since their formation mechanism is not described by the standard FPM forward model. This results in a strong mismatch between the estimated and experimentally acquired intensity images. The rdFPM model proposed in the main manuscript explicitly accounts for spherical illumination. However, it does not incorporate vignetting effects, and therefore the PB/PD images generated by the rdFPM forward model may still differ from those observed experimentally. To mitigate such residual system–model discrepancies, the IIC update procedure was introduced.

To investigate the influence of IIC in the presence of PB/PD images, we simulated a series of FPM datasets using the rdFPM forward model while varying the LED-sample distance l_z between 1.5 mm and 50 mm. For each value of l_z, the LED lateral spacing was adjusted accordingly (from 0.2 mm to 6.67 mm) in order to maintain identical illumination angles across all datasets. The simulated object consisted of phase USAF targets, as in Fig. S9. All remaining system parameters were kept consistent with the experimental setup (10×/0.25 NA objective, 3.45 μm pixel pitch, 1440×1080 camera resolution, 9×9 LED array, $\lambda = 535$ nm). This procedure produced a family of datasets that differ only in wavefront curvature and, consequently, in the occurrence of PB/PD images. The mosaics of the generated datasets are shown in Fig. S5. As expected, increasing the wavefront radius (larger l_z) reduces the prevalence of PB/PD images. Their number decreases from 24 for $l_z = 1.5$mm, to 4 for $l_z = 7$mm, and they disappear entirely for $l_z = 50$mm, corresponding to near-plane-wave illumination.

Next, all generated datasets were reconstructed using the standard FPM algorithm, both with and without the IIC update (Fig. S6). This intentionally creates a model mismatch scenario in which datasets containing PB/PD images (generated under spherical illumination) are reconstructed using a plane-wave-based FPM forward model. Figure S6(a) presents the reference reconstruction obtained for plane-wave-generated data ($l_z \to \infty$). Figure S6(c) shows the full field-of-view reconstructions for different l_z values, obtained using FPM and FPM+IIC. Zoomed-in regions from the central, upper, and upper-right parts of the field of view are presented in Fig. S7, and the corresponding phase RMSE values are shown in Fig. S6(b). As observed, reconstruction accuracy decreases both with decreasing l_z (i.e., increasing wavefront curvature) and with increasing distance from the center of the FOV. Importantly, incorporating the IIC update substantially improves reconstruction quality in all analyzed cases, both qualitatively (Fig. S7) and quantitatively (Fig. S6(b)), despite the fact that IIC does not explicitly model spherical illumination in the forward model. These results demonstrate that IIC effectively suppresses reconstruction errors associated with the presence of PB/PD images.

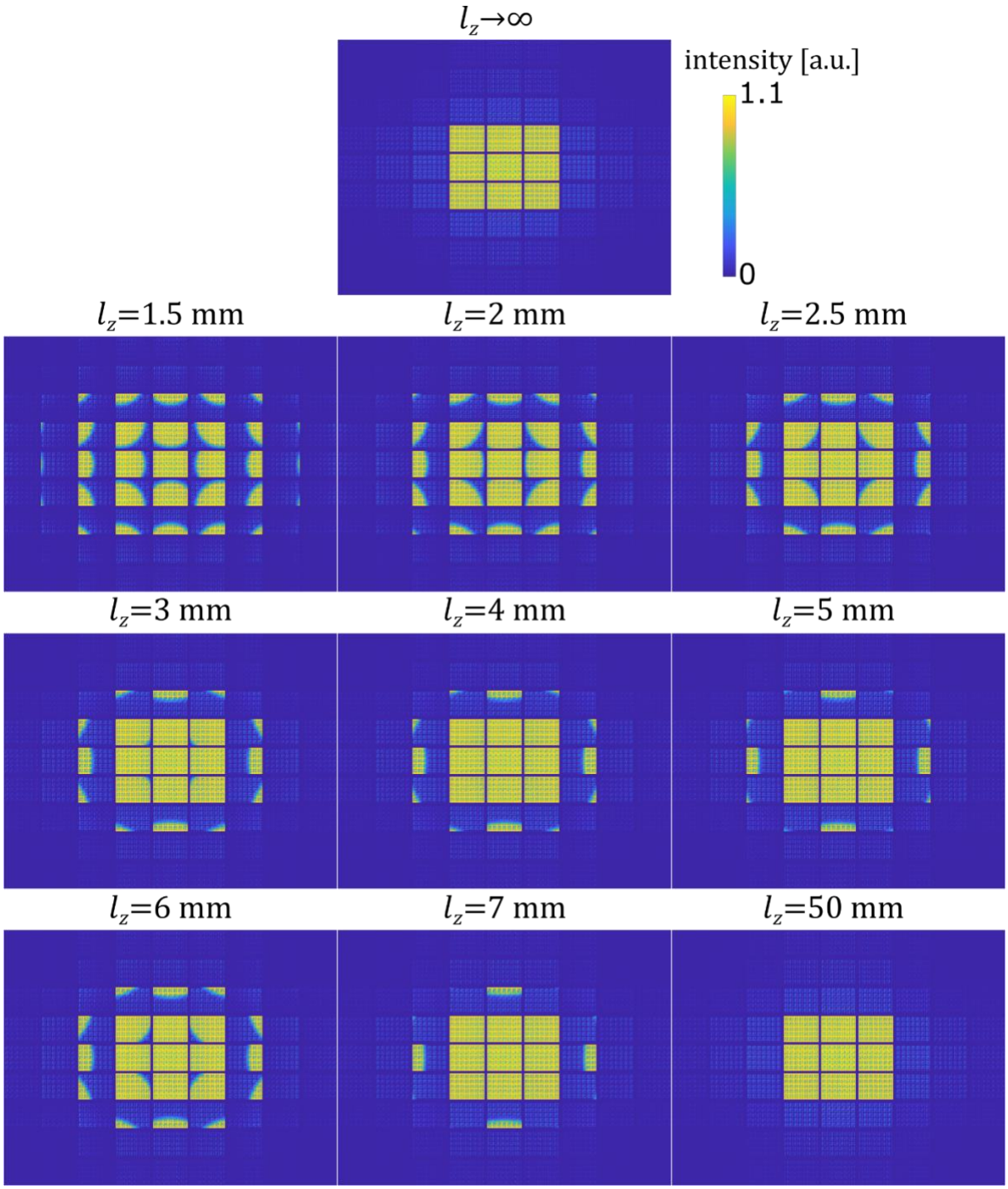

Fig. S5. A set of mosaics of simulated FPM datasets generated for varying LED-sample distances l_z, while maintaining identical illumination angles across datasets. Increasing l_z increases the wavefront radius and reduces the number of PB/PD images. The simulated object consists of phase USAF targets from Fig. S9.

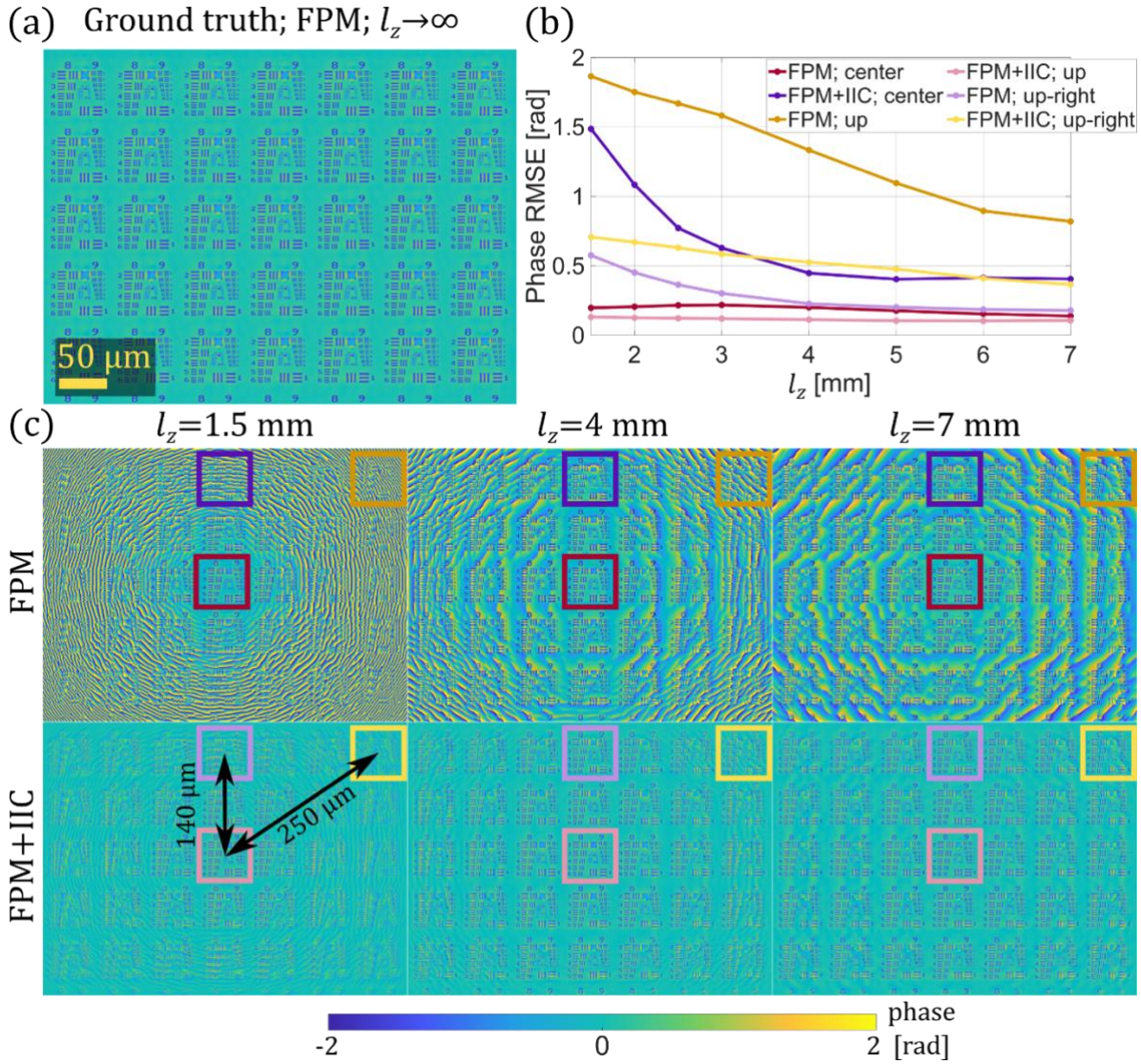

Fig. S6. Reconstructions of the datasets shown in Fig. S5. (a) Reference reconstruction obtained from plane-wave-generated data using the standard FPM algorithm. (b) Phase root-mean-squared error as a function of l_z, calculated for the regions of interest (ROIs) shown in Fig. S7. (c) Full FOV reconstructions obtained using standard FPM and FPM+IIC algorithms for spherical-wave-generated datasets. Colored squares indicate the ROIs enlarged in Fig. S7.

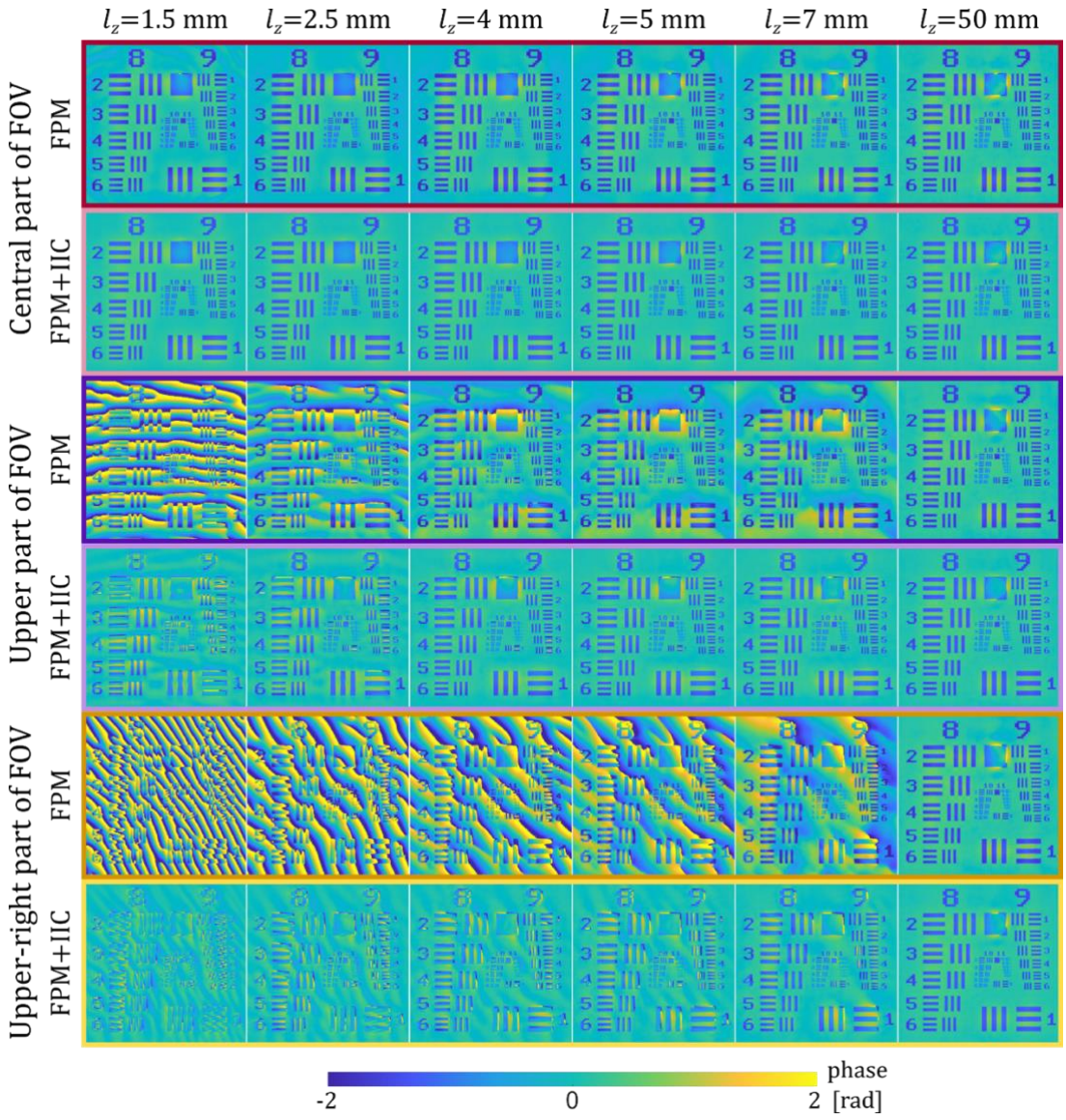

Fig. S7. Enlarged regions of interest from the reconstructions shown in Fig. S6, corresponding to the central, upper, and upper-right parts of the field of view.

6. Detailed analysis of results from main manuscript Figures 5-8

In the main manuscript Fig. 5, we demonstrated for amplitude-type sample that standard FPM entirely fails under extreme near-field illumination, whereas our proposed rdFPM+IIC framework achieves high-fidelity, artifact-free reconstructions across the entire FOV even in the misaligned systems. Here, Figure S8 present the enlarged images from manuscript Fig. 5 for better visualization.

Figure S9 present the additional simulation, performed for the same parameters as in the main manuscript Fig. 5 but with object simulated as a phase test targets with phase values scaled in [-2, 0] rad range. The reconstruction results are analogous to the amplitude-only sample: the FPM exhibit strong distortion-errors in the vast majority of retrieved FOV and supporting it with IIC can

partially mitigate those errors but still exhibit strong inaccuracies near FOV border. The rdFPM reconstruct the phase accurately for the well-aligned data, but for the misaligned data it starts introducing distortion errors – those errors can be minimized via supporting the rdFPM with the IIC procedure.

The main difference between amplitude and phase sample reconstruction lies in the characteristic of the distortion errors. For amplitude reconstructions those distortions manifest in a fringe-like shape (Fig. S8(c)), while in the phase result they manifest as the phase wraps (Fig. S9(c)). Importantly, those phase wraps cannot be directly unwrapped as they often become discontinues, which makes the phase unwrapping process unambiguous – e.g., in light-cyan zoomed-in area in Fig. S9(c2) the phase wrap line that starts from bottom-right part of the image, vanishes near its center.

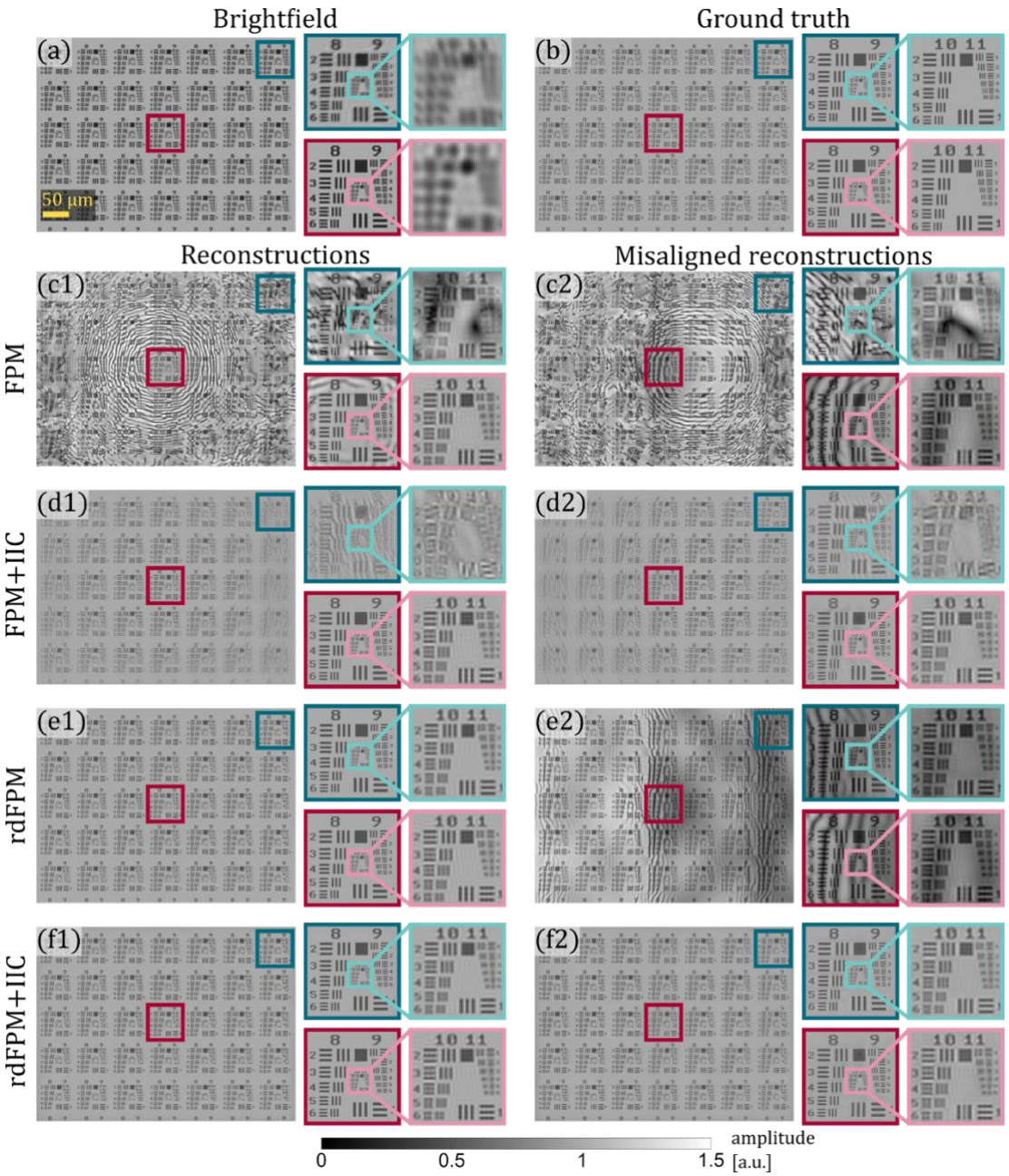

Fig. S8. Numerical simulations – amplitude sample. (a) Brightfield image. (b) Ground truth amplitude. (c1)-(f1) Amplitude reconstructions in perfectly aligned system. (c2)-(f2) Amplitude reconstructions in misalignment system – LED array shifted in x direction by $\Delta l_x = 50\ \mu m$.

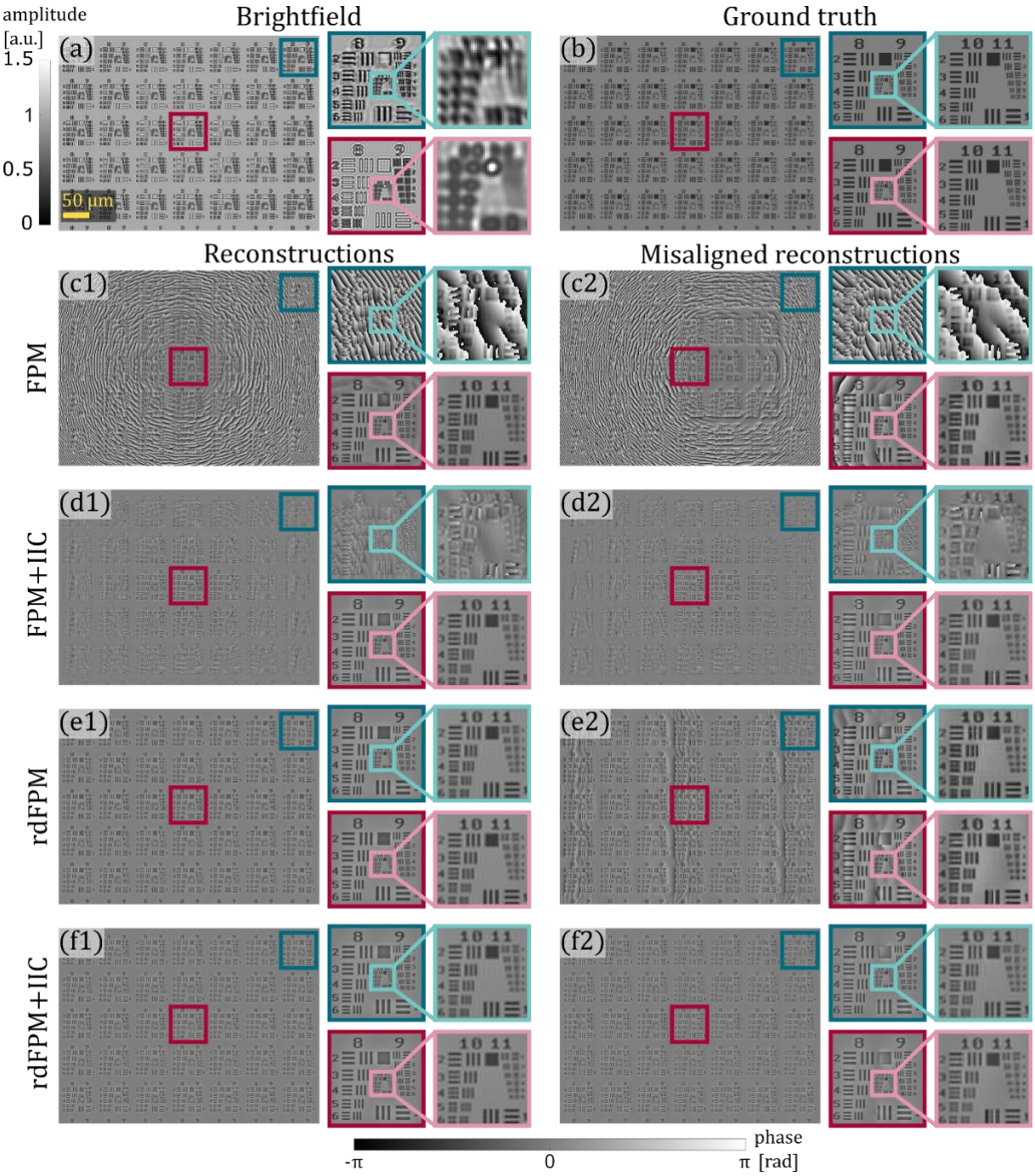

Fig. S9. Numerical simulations – amplitude sample. (a) Brightfield image. (b) Ground truth phase. (c1)-(f1) Phase reconstructions in perfectly aligned system. (c2)-(f2) Phase reconstructions in misalignment system – LED array shifted in x direction by $\Delta l_x = 50\ \mu m$.

In the main manuscript Fig. 6 we evaluated the algorithms performance by measuring the USAF amplitude resolution target with two different microscope objectives: 2×/0.1 and 10×/0.25 – where for the 10× objective the USAF target was placed in two different lateral positions – firstly with smallest USAF groups in the central position of measured FOV and then with those groups moved to the corner part of FOV.

Here in the Fig. S10 there are shown enlarged full FOV reconstructions from this experiment, while in Figure S11 there are presented enlarged regions of interests with smallest USAF groups – marked with dark cyan rectangles in Figs. S10(a). For a more complete comparison, both figures

include also the FPM+IIC and rdFPM reconstructions, that were skipped in main manuscript Fig. 6.

In Figs. S10(a) and S11(a) there are shown the microscope images acquired with central LED illumination, where only the limited spatial resolution is observed. For 2× objective, the smallest resolvable test lines are from group 7, element 6 (2.19 μm wide), Fig. 8(a1), while for 10× objective and object placed in the image center there are visible lines from group 9 element 1 (0.98 μm wide), Fig. S11(a2). Both values are slightly below diffraction limited resolution (λ/2NA equals 2.7 and 1.1 μm respectively), probably due to not high enough NA of the illumination. For 10× objective and object placed near image corner the observed image resolution is even higher (group 9 element 3 – 0.78 μm wide), as due to spherical illumination wavefront, in the corner part of FOV the effective illumination NA is significantly higher than for the central part of the FOV.

Figures S10(b) and S11(b) show the reconstructions obtained with FPM technique, where significant distortions are observed both globally in full FOV and locally in zoomed-in area. Those errors are significantly minimized after applying the proposed IIC support to the FPM reconstruction (Figs. S10(c), S11(c)). However, this reconstruction improvement is observed only in the central part of reconstructed FOV (Figs. S11(c1), S11(c2)), where the assumed plane wave illumination matches well with the central part of the actual spherical illumination wavefront. For 2× objective there is observed information vanishing far from the central part of FOV, Fig. S10(c1), while for 10× objective and object placed in corner part of FOV there are observed significant distortions that negatively affect the reconstruction accuracy and resolution, Fig. S11(c3).

Figures 7(d) and 8(d) present the reconstructions with proposed rdFPM model, where the overall image distortions are significantly smaller than for the FPM standalone method. However, they are still observable, especially in the areas where the brightfield-darkfield borders occur in subsequent images – visible as white rings in Fig. S10(d1) of the diameter of brightfield area from Fig. S10(a1), or like the fringe-like errors in Figs. S10(d2), S10(d3). Those errors result from the intensity mismatch between the registered images I_n and the estimated ones E_{est_n} during the reconstruction. After supporting rdFPM with proposed IIC update method (Figs. S10(e), S11(e)), the reconstructions errors due to intensity mismatch are significantly minimized, resulting in high resolution and high accuracy reconstructions within the whole measured FOVs.

For the proposed rdFPM + IIC method, the smallest resolvable lines were from group 9 element 3 (0.78 μm wide) for 2× objective and from group 10 element 3 (0.39 μm wide) for 10× objective, which matches well with the theoretical resolution of 0.70 μm and 0.38 μm for those objectives, respectively (synthetic NA were 0.38 and 0.71, respectively). FPM + IIC achieved the same resolution as rdFPM + IIC only when test was placed in the central part of FOV (Figs. S11(c1), S11(c2)), while for object corner placement the resolution was definitely worsened but hard to precisely estimate due to image distortions. FPM and rdFPM achieved same resolution as rdFPM + IIC for 2× objective and slightly worsened (to 0.44 μm wide lines) for 10×objective, which indicates that low frequency errors and image distortions might also negatively affect the high frequency details reconstruction.

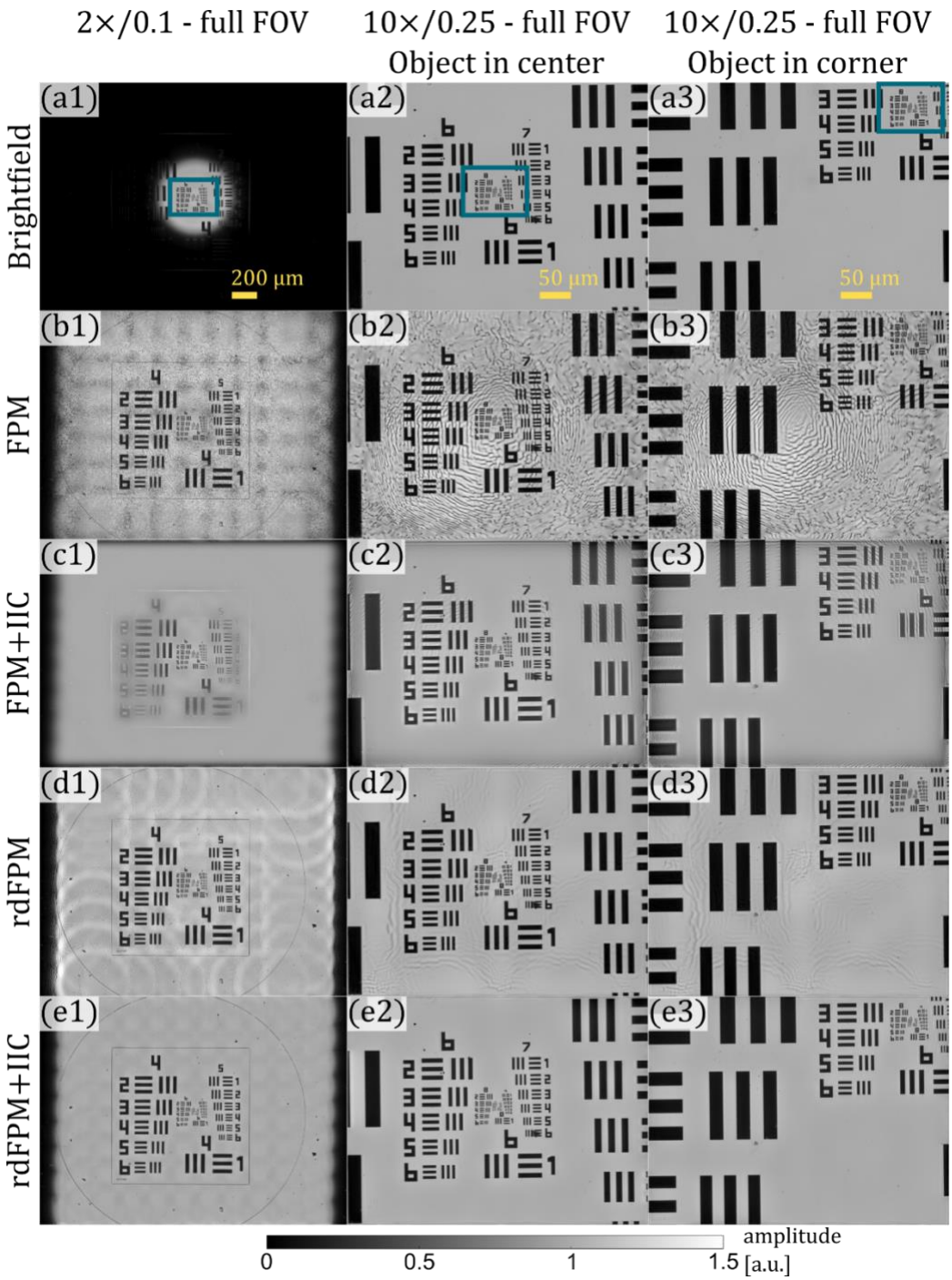

Fig. S10. Experimental results – USAF amplitude test target. Images are shown in full FOV. Areas marked with dark-cyan rectangles in (a) are shown enlarged in Fig. S11.

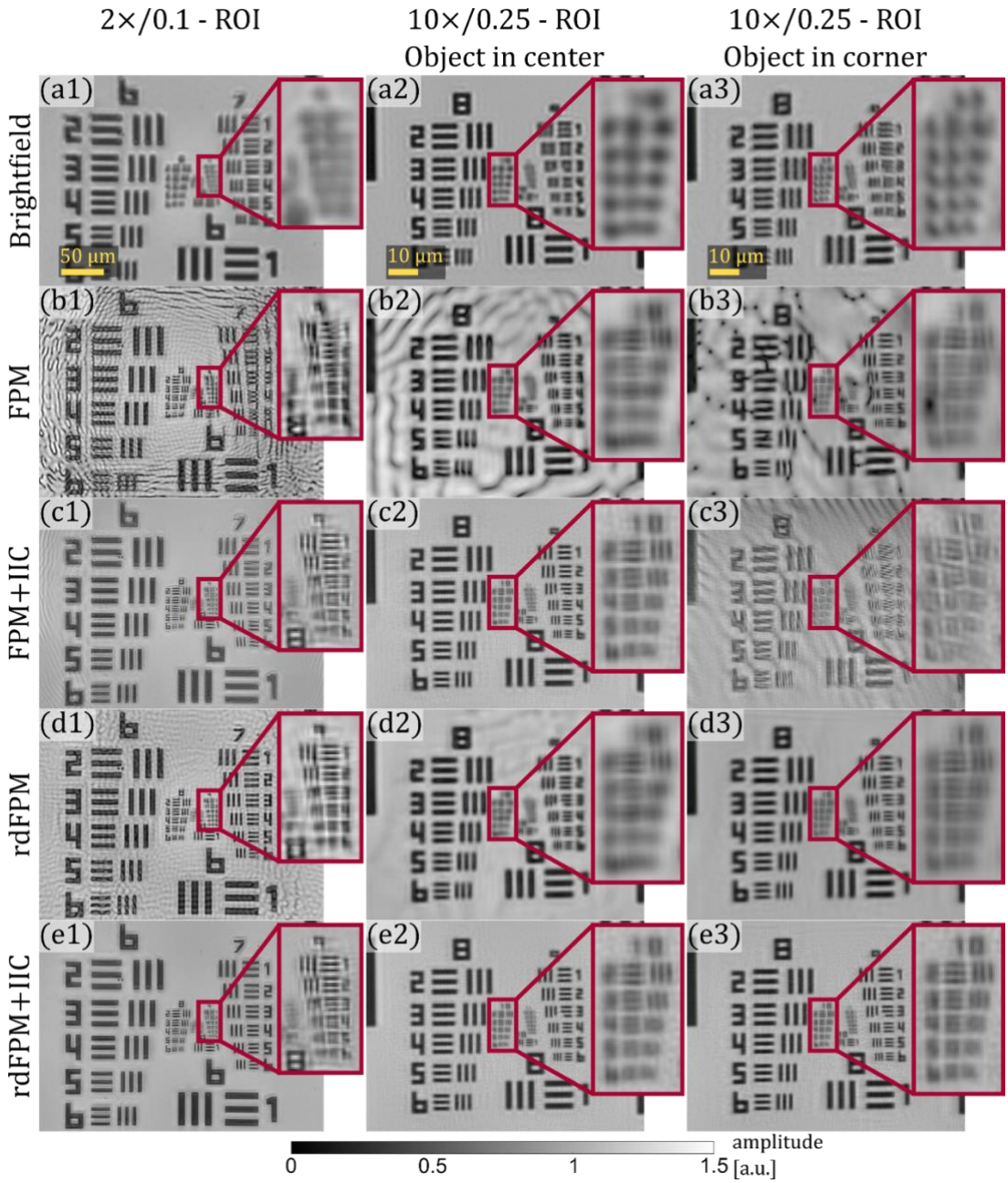

Fig. S11. Experimental results – USAF amplitude test target. Shown region of interests with smallest USAF groups. Full FOV reconstructions are presented in Fig. S10.

The necessity of the combined rdFPM+IIC framework is most evident in the highly transparent biological samples. In the main manuscript we showed the phase reconstructions for Lenti-X 293T cells (Fig. 7) and Wistar rat neuronal cells (Fig.8). Here, in Figs. S12 and S13 we show the enhanced versions of manuscript Figs. 7 and 8 respectively, where the FPM, FPM+IIC and rdFPM results are shown in full resolution, enabling their more advanced qualitative comparison with rdFPM+IIC result.

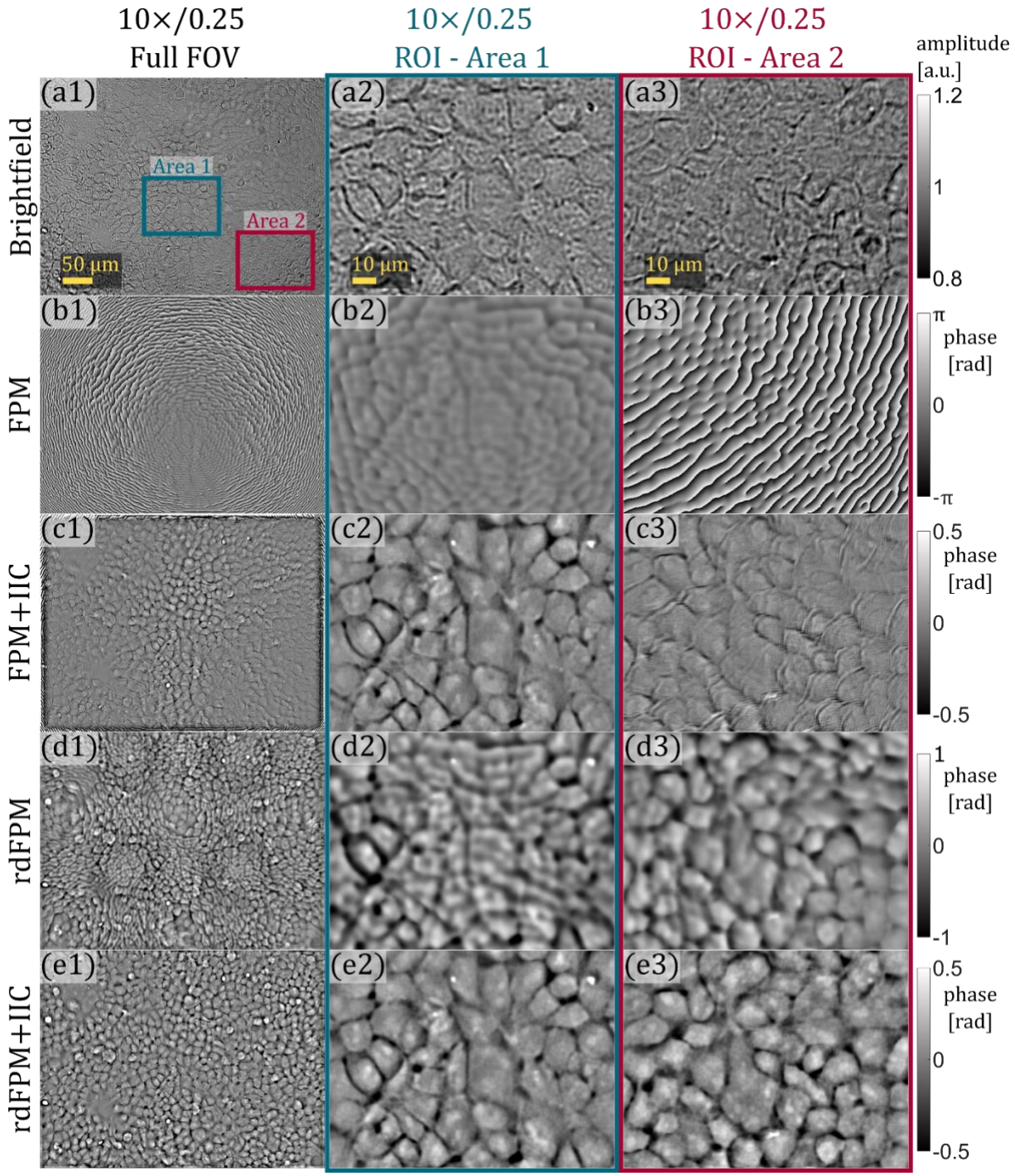

Fig. S12. Phase reconstruction of Lenti-X 293T cells cells utilizing a 10×/0.25 NA objective. (a1) Brightfield intensity images showing low overall contrast. Images (a1)-(e1) show the full FOV, while images in column (a2)-(e2) correspond to the blue Area 1 and images in column (a3)-(e3) correspond to the red Area 2. (b) Standard FPM phase reconstructions, showing spherical-like aberrations. (c) FPM reconstruction with addition of IIC. While low-frequency errors are minimized in the central FOV, phase information vanishes toward the image borders, accompanied by fringe-like artifacts. (d) rdFPM reconstruction. Artifacts seen in (b) are reduced, but the phase remains obscured by low-frequency artifacts that blur cellular details. (e) rdFPM+IIC reconstruction, demonstrating accurate, high-fidelity phase recovery across the entire FOV without any noticeable reconstruction errors or distortions.

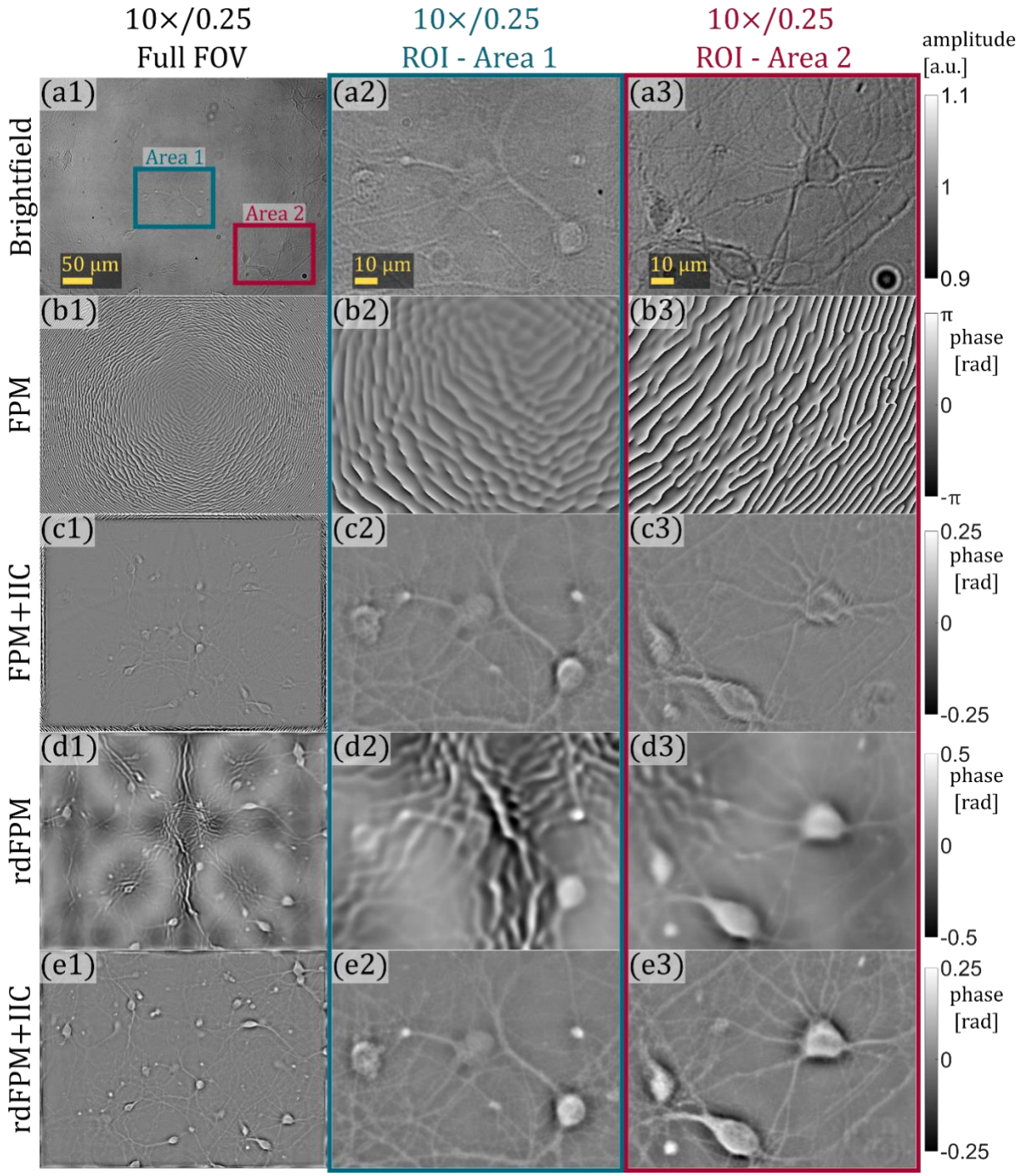

Fig. S13. Phase reconstruction of highly transparent Wistar rat neuronal cells obtained for 10×/0.25 NA objective (a1) Brightfield intensity images showing low overall contrast. Images (a1)-(e1) show the full FOV, while images in column (a2)-(e2) correspond to the blue Area 1 and images in column (a3)-(e3) correspond to the red Area 2. (b) Standard FPM phase reconstructions, showing spherical-like aberrations. (c) FPM reconstruction with addition of IIC. While low-frequency errors are minimized in the central FOV, phase information vanishes toward the image borders, accompanied by fringe-like artifacts. (d) rdFPM reconstruction. Artifacts seen in (b) are reduced, but the phase remains obscured by low-frequency artifacts that blur cellular details. (e) rdFPM+IIC reconstruction, demonstrating accurate, high-fidelity phase recovery across the entire FOV without any noticeable reconstruction errors or distortions.